Quarterly Journal of the Royal Meteorological Society *Q. J. R. Meteorol. Soc.* **00: 1–15 (2019)**

Weak- and Strong-Friction Limits of Parcel Models: Comparisons and Stochastic Convective Initiation Time†

Gerardo Hernandez-Duenas*[a], Leslie M. Smith[bc], and Samuel N. Stechmann[bd]

[a]*Instituto de Matemáticas, Universidad Nacional Autónoma de México - Campus Juriquilla, Querétaro, México*

[b]*Department of Mathematics, University of Wisconsin - Madison, Madison, Wisconsin, USA*

[c]*Department of Engineering Physics, University of Wisconsin - Madison, Madison, Wisconsin, USA*

[d]*Department of Atmospheric and Oceanic Sciences, University of Wisconsin - Madison, Madison, Wisconsin, USA*

*Correspondence to: Instituto de Matemáticas
Universidad Nacional Autónoma de México - Campus Juriquilla, Querétaro, México
E-mail: hernandez@im.unam.mx

For moist convection, models of individual parcel dynamics are valuable for their simple formulation and predictions of cloud properties. Here, two limiting idealized cases of parcel theory are investigated: the weak- and strong-friction limits. The weak-friction limit is a traditional limit with no momentum drag, and the dynamics are a Hamiltonian system for the parcel's height and vertical velocity. A strong-friction limit is derived and studied here, and its limiting form involves a balance between frictional drag and buoyancy, which provides a differential equation for parcel height as a function of time. In the two limiting regimes, analytical formulas are presented and compared for quantities such as maximum vertical velocity and cloud-top height. For example, in the strong-friction limit, the cloud-top height coincides with the level of neutral buoyancy (LNB), whereas in the weak-friction limit the cloud-top height is far above the LNB. This comparison suggests the strong-friction limit may provide more realistic predictions of some averaged cloud properties. In general, since frictional effects and individual parcel properties can vary even within a single cloud, the predictions of the weak- and strong-friction limits can be viewed as upper and lower bounds for the behavior of more realistic finite-friction scenarios. Finally, in a stochastic version of the parcel model, in the strong-friction limit, analytical formulas are derived for convective initiation time. Applications to convective parameterizations are discussed; for example, the formulas for convective initiation time could be applied as stochastic convective triggers.

Key Words: Parcel models, plume models, stochastic dynamics, adiabatic parcel

Received . . .

1. Introduction

Moist convection and cloud dynamics are complex processes, and simple theories have long been sought after. In one simplified perspective, moist convection is viewed in terms of fluid parcels (e.g., Simpson and Wiggert 1969; Brast *et al.* 2016). In the most idealized scenario, each parcel rises as an undiluted, undamped entity, with its vertical velocity generated through the parcel's buoyancy. Since this idealized scenario neglects momentum damping, we will call it the weak-friction limit.

In this paper, the main goal is to derive and investigate the dynamics of the opposite limit: the strong-friction limit. In this limit, the parcel's vertical motion is strongly damped, and the vertical acceleration is relatively small, which leaves a dominant balance between frictional drag ($\tau_w^{-1}w$), buoyancy (b), and other forcing (f):

$$\frac{1}{\tau_w}\frac{dz}{dt} = b(z) + f. \qquad (1)$$

(If the frictional drag is parameterized in a form other than $\tau_w^{-1}w$, then a similar balance and similar differential equation for height $z(t)$ could be derived, although its detailed form would be different.)

The overarching questions of the present paper are: Can analytical formulas be derived in the strong-friction limit? Based on the analytical formulas, what are the cloud and parcel properties that are predicted in the strong-friction limit? How do the predictions of the strong-friction limit compare with predictions of the weak-friction limit? Analytical formulas are one

†Investigación realizada gracias al Programa UNAM-DGAPA-PAPIIT IN113019
Research supported in part by grant UNAM-DGAPA-PAPIIT IN113019

of the valuable aspects of the weak-friction limit, and analytical formulas for the strong-friction limit could potentially provide the idealized counterpart of the well-known weak-friction limiting dynamics.

Some interesting studies have used large eddy simulations to investigate the strength of frictional drag on fluid parcels. Some results suggest that friction may be weak, a scenario they call "slippery thermals" (Sherwood *et al.* 2013). Other results suggest that friction may be strong, a scenario they call "sticky thermals" (Romps and Charn 2015). Nature may perhaps involve a complex variety of scenarios (Hernandez-Deckers and Sherwood 2016). In the present study, the goal is not to assess the strength of frictional drag, but to examine the idealized parcel models that arise in the two extreme cases of the weak- and strong-friction limits.

As one main theme here, the properties of an adiabatic, rising parcel are derived in the strong-friction limit. For example, the vertical velocity profile can be written analytically in terms of parameters such as the environmental moist thermodynamic profile. Compared to the traditional weak-friction limit, an adiabatic strong-friction parcel reaches its maximum vertical velocity at a much lower altitude. One would expect the weak- and strong-friction limits to be useful for upper and lower bounds on predictions of cloud properties, with the more realistic finite-friction dynamics lying in between.

Another main quantity of interest here will be *convective initiation time*, the time elapsed in waiting for a boundary-layer parcel to reach a barrier located above in the vicinity of the level of free convection. In the strong-friction limit, in a stochastic version of the model, an approximation of the mean convective initiation time can be found in analytic form. Such an analytic formula could be applied in convective parameterizations as a simple stochastic trigger (Kain and Fritsch 1992; Lin and Neelin 2000; Majda and Khouider 2002; Jakob and Siebesma 2003; Stechmann and Neelin 2011, 2014; Gentine *et al.* 2013a,b; D'Andrea *et al.* 2014; Hottovy and Stechmann 2015). Indeed, one of the main applications of parcel and plume models is to convective parameterizations.

The rest of the paper is organized as follows. The parcel model for convection is described in section 2, and some motivating examples of parcel pathways are illustrated in section 3. Then, in sections 4 and 5, derivations of the weak- and strong-friction limits are described, and their parcel properties are compared in terms of vertical velocity, cloud-top height, etc. Convective initiation time is investigated in a stochastic version of the parcel model in section 6, including approximations that allow for analytical formulas. Finally, sections 7 and 8 present some additional discussion and conclusions.

2. Model description

As a simple model of moist convection, the dynamics of a parcel will be given by the stochastic differential equation (SDE)

$$\begin{aligned} dz &= w\,dt, \\ dw &= b\,dt \quad -\tfrac{1}{\tau_w} w dt \quad + b_w dW. \end{aligned} \tag{2}$$

Here, z and w are the parcel's height and vertical velocity at time t, respectively. The fluid dynamical interactions between the parcel and the rest of the atmosphere is incorporated with a simple relaxation in the vertical velocity $(-w/\tau_w)$ and a stochastic term $(b_w dW)$. Physically, one contributor to the relaxation could be entrainment—the mixing process between the parcel and the environment—although other significant contributions could come from in-cloud fluid dynamical effects. Here τ_w is the relaxation timescale for the vertical velocity, which is relaxed toward the zero vertical velocity of the parcel's surroundings. Intuitively, and in brief, dW is a random forcing. The infinitesimal Wiener increment dW is the limit of the small increment $\Delta W = W(t+\Delta t) - W(t)$, in the limit as $\Delta t \to 0$, in much the same way that dz is the limit of $\Delta z = z(t+\Delta t) - z(t)$. For finite Δt, a new value of ΔW is chosen at each time step, and each value is an independent sample from a Gaussian distribution with mean 0 and variance Δt. In the limit of $\Delta t \to 0$, the SDE is obtained and it is interpreted here in the Ito sense (Gardiner 2004). Furthermore, the buoyancy b is given by

$$b = \frac{g}{\theta_o}\left(\theta_{\mathrm{v}} - \theta_{\mathrm{v,env}}\right), \tag{3}$$

where $g = 9.81$ m s^{-2} is the acceleration of gravity, $\theta_o = 300$ K is a reference value of the potential temperature at sea surface, and θ_{v} and $\theta_{\mathrm{v,env}}$ are the virtual potential temperatures of the parcel and environment, respectively, which are to be specified further below in Section 2.1.

Note that the parcel's thermodynamic properties are assumed to be conserved – i.e., it is an adiabatic parcel model. While such an assumption may not be realistic, it is a convenient simplification that is commonly used (e.g., Xu and Emanuel 1989; Emanuel 1994; Grabowski and Jarecka 2015) and allows for the derivation of some analytical formulas. The possibility of modeling non-adiabatic parcel dynamics is discussed below in section 7.

One difference from typical parcel models is that the model here is time dependent. For instance, other stochastic parcel models have been considered in the past (e.g., Fraedrich 1985), although without time dependence. A time-dependent model is needed for the analysis of certain quantities of interest, such as the time it takes for a parcel to reach a barrier located above in the vicinity of the level of free convection (convective initiation time), and we will show below that explicit approximations can be obtained under certain conditions.

2.1. *Simplified thermodynamic relations*

The model in (2)–(3) can be closed by defining both the environment- and parcel- virtual potential temperatures, $\theta_{\mathrm{v,parcel}}$ and $\theta_{\mathrm{v,env}}$. To this end, we will use linearized versions of the full thermodynamic relations (Majda and Xing 2010; Deng *et al.* 2012; Hernandez-Duenas *et al.* 2013). Such relations simplify the model significantly compared to more comprehensive thermodynamics relations, since they allow explicit formulas to be obtained in many situations, as seen below. However, we have also investigated more comprehensive thermodynamic relations, and the main results of this paper are essentially the same, although some results can then only be obtained numerically, not analytically, so we instead focus here on the simplified, linearized thermodynamics.

In this spirit, the virtual potential temperature is given by

$$\theta_{\mathrm{v}} = \theta_{\mathrm{e}} + \theta_o\left(\epsilon_o - \frac{L}{c_p\theta_o}\right) q_{\mathrm{v}} - \theta_o q_\ell. \tag{4}$$

Here θ_e is the equivalent potential temperature, q_v, q_ℓ the water vapor and liquid water mixing ratios, $c_p = 10^3$J kg^{-1}K^{-1} the specific heat at constant pressure, $L = 2.5\times 10^6$ J kg^{-1} is the latent heat of vaporization, and $R_v/R_d = 1+\epsilon_o$ is the ratio of gas constants for water vapor (R_v) and dry air (R_d) with $\epsilon_o \approx 0.6$. This formula can be used, as described below, to define the parcel and environmental θ_{v} values by inserting parcel and environmental values, respectively, into the right-hand side.

The parcel will be assumed to be adiabatic in the sense that its total water q_t and equivalent potential temperature θ_e are assumed to be conserved and not changing in time. We will assume that there is neither precipitation nor formation of rain. All the water that is condensed is kept with the parcel, leaving

Table 1. Simplified thermodynamic relations.

Env. quantities	
$\theta_o = 300K$, $B = 3\text{K km}^{-1}$	$\theta_{\text{env}}(z) = \theta_o + Bz$
$q_{\text{v,env}}(z)$	$\theta_{\text{e,env}}(z) = \theta_{\text{env}}(z) + \frac{L}{c_p} q_{v,\text{env}(z)}$
	$\theta_{\text{v,env}}(z) = \theta_{e,\text{env}(z)}$ $+\theta_o\left(\epsilon_o - \frac{L}{c_p\theta_o}\right) q_{\text{v,env}}(z)$
Parcel quantities	Definition
z, w	Height and vertical velocity.
θ_e	Equivalent pot. temperature.
q_t	Total water mixing ratio.
Relations	Comments:
$p(z)$	Total pressure as a function of height only.
$q_{\text{vs}}(z)$	Water vapor at saturation as a function of height only.
$q_v = \min(q_t, q_{\text{vs}})$	Water vapor mixing ratio.
$q_\ell = \max(q_t - q_{\text{vs}}, 0)$	Liquid water mixing ratio.
$\theta_{\text{v}} = \theta_{\text{e}} - \theta_O q_\ell$ $+\theta_O\left(\epsilon_O - \frac{L}{c_p\theta_O}\right) q_{\text{v}}$	Virtual potential temperature
$b = \frac{g}{\theta_o}(\theta_v - \theta_{\text{v,env}})$	Buoyancy

the total water $q_t = q_v + q_\ell$ constant, as in a reversible process. The presence of rain fallout would increase the parcel's virtual potential temperature and increases the cloud top height. We have explored those situations with different rainfall speeds in the model (not shown) and no qualitative differences have been observed other than the one mentioned above. In the spirit of a simplified setting, we then only consider two constituents of water: water vapor and cloud liquid water. As part of the simplified thermodynamics, we also assume a saturation water vapor $q_{\text{vs}}(z)$ as a function of height only. The dependence on z is chosen to be a function with roughly exponential decay, as used in Hernandez-Duenas *et al.* (2013). The water vapor and liquid water are then given by

$$q_v = \min(q_t, q_{\text{vs}}(z)), q_\ell = \max(q_t - q_{\text{vs}}(z), 0). \quad (5)$$

We have also explored other choices. For instance, extracting all the condensed water instantaneously from the parcel can be interpreted as having a vanishing liquid water, as in a pseudoadiabatic process. We note that such a scenario results in a slightly higher cloud top height. However, there is no qualitative differences compared to the previous case.

Plots of the environmental thermodynamic profiles are shown here in Fig. 1. The environmental potential temperature $\theta_{\text{env}}(z) = \theta_o + Bz$ is taken to be linear with respect to height with rate $B = 3\text{ K km}^{-1}$. With these choices, the environmental -equivalent and -virtual potential temperature are

$$\begin{aligned} \theta_{\text{e,env}}(z) &= \theta_{\text{env}}(z) + \tfrac{L}{c_p} q_{\text{v,env}}(z), \\ \theta_{\text{v,env}}(z) &= \theta_{\text{e,env}}(z) + \theta_o\left(\epsilon_o - \tfrac{L}{c_p\theta_o}\right) q_{\text{v,env}}(z). \end{aligned} \quad (6)$$

Table 1 includes all the variables and the simplified thermodynamic relations.

The virtual potential temperature fluctuation, $\theta_{\text{v}} - \theta_{\text{v,env}}$, is then an explicit function of height, given by

$$\begin{aligned} \theta_v'(z) &= \theta_{\text{e}} - \theta_{\text{e,env}}(z) \\ &+ \theta_o\left(\epsilon_o - \frac{L}{c_p\theta_o}\right)(q_{\text{v}}(z) - q_{\text{v,env}}(z)) - \theta_o q_\ell(z), \end{aligned} \quad (7)$$

and the buoyancy from (3) can likewise now be defined accordingly as an explicit function of height:

$$b(z) = \frac{g}{\theta_o}\theta_v'(z). \quad (8)$$

This completes the specification of the model.

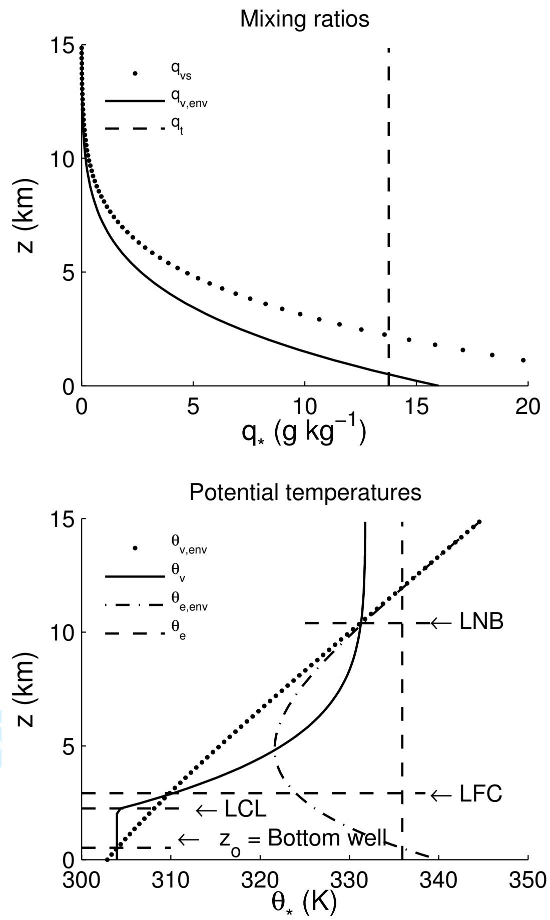

Figure 1. Top: Mixing ratios showing total water (dashed curve), environmental water vapor (solid line) and water vapor at saturation (dots). Bottom: Virtual and equivalent potential temperatures for environment and parcel. The symbols for each temperature are specified in the legend.

To define the initial conditions, the parcel is initially located at a height z_o and its thermodynamic properties are assumed to be in balance with its environment, i.e., the equivalent potential temperature and moisture of the parcel and the environment coincide $\theta_e = \theta_{e,\text{env}}(z_o)$, $q_{\text{v}} = q_{\text{v,env}}(z_o)$. As a consequence, the virtual potential temperatures are also initially in balance $\theta_v = \theta_{v,\text{env}}(z_o)$. Here we choose this initial height z_o to be close to the surface: $z_o = 0.5$ km. Fig. 1 shows the profiles for water vapor (top panel) and the equivalent and virtual potential temperatures (bottom panel) where one can corroborate the intersection of the profiles at the initial parcel's height.

For a rising parcel, three heights are particularly important, and while they are well-known, it is useful to briefly summarize them here to facilitate further discussions below. Fig. 1 (bottom panel) shows the three heights, and it also illustrates that the three heights mark transitions between positive and negative buoyancy. In particular, as a parcel first rises from the boundary layer, its virtual potential temperature is conserved up until the *lifting condensation level* (LCL), which is the level where the parcel's water vapor starts to condense (see the bottom panel of Fig. 1). Since the environmental virtual potential temperature increased during all this time, the parcel becomes negatively buoyant. However, if the parcel continues to rise above the lifting condensation level, its virtual potential temperature increases and it could intersect with the environmental virtual potential temperature again. The height where it occurs is known as the *level of free convection* (LFC). The parcel becomes positively buoyant again above the LFC and can continue rising without any other forcing assuming it was able to reach such a height. Finally, the buoyancy vanishes again at the so called *level of neutral buoyancy* (LNB). The level of neutral buoyancy is sometimes related to the cloud top height. In reality, it is the place where the parcel starts decelerating due to buoyancy. Depending on the properties of the system (like mixing with the environment), LNB could provide one estimate for the cloud top height or the parcel could go much higher up. We will analyze such situations in more detail in Section 5.

2.2. *Potential energy and total energy*

It will be useful to define a total energy E of the system, and to relate it to the concepts of CIN and CAPE (to be described below). The total energy is defined as

$$E(z,w) = \frac{1}{2}w^2 + \Pi(z), \tag{9}$$

which is an explicit function of height and vertical velocity. The first term, $w^2/2$, is the kinetic energy, and the second term,

$$\Pi(z) = \frac{g}{\theta_o}\int_z^H \theta_v'(z')dz' \tag{10}$$

is the potential energy of the system. Here $H = 15\,\text{km}$ is the troposphere's depth. The mass m of the parcel is here assumed to be constant. We note that we have re-scaled the actual energy $\frac{1}{2}mw^2 + m\Pi(z)$ by the constant mass m (see Section 4.1 for further discussion).

The concepts of convective inhibition (CIN) and convective available potential energy (CAPE) are related to the potential energy $\Pi(z)$, as illustrated in the bottom panel of Fig. 2. The figure shows that $\Pi(z)$ is a double well potential. The bottom well has a local minimum at the parcel's initial height, z_o. The upper well has a local minimum at the LNB. In between the two wells is a metastable local maximum (a saddle point) at the LFC. The convective inhibition

$$\text{CIN} = \Pi(z_o) - \Pi(\text{LFC}) \tag{11}$$

is a measure of the depth of the bottom well, and it is defined as the potential energy difference between the bottom of the well and the level of free convection. It is negative and is associated with the amount of potential energy that the parcel would need to convert to kinetic energy in order to escape from the bottom well. On the other hand, the convective available potential energy

$$\text{CAPE} = \Pi(\text{LFC}) - \Pi(\text{LNB}) \tag{12}$$

is a measure of the depth of the upper well, and it is defined as the potential energy difference between the bottom of the upper well and the saddle point. In the plot, vertical dashed lines were included to identify CIN and CAPE more clearly. The parameter values that we chose give $\text{CIN} = -152.68\,\text{J kg}^{-1}$ and $\text{CAPE} = 1214.2\,\text{J kg}^{-1}$. A value of $|CIN|$ greater than $200\,\text{Jkg}^{-1}$ can be sufficient to prevent convection in the atmosphere. The value of CAPE reported here is about one quarter the values that are reported for extreme events. We also note that the upper well is much deeper than the bottom one. This depth's difference has

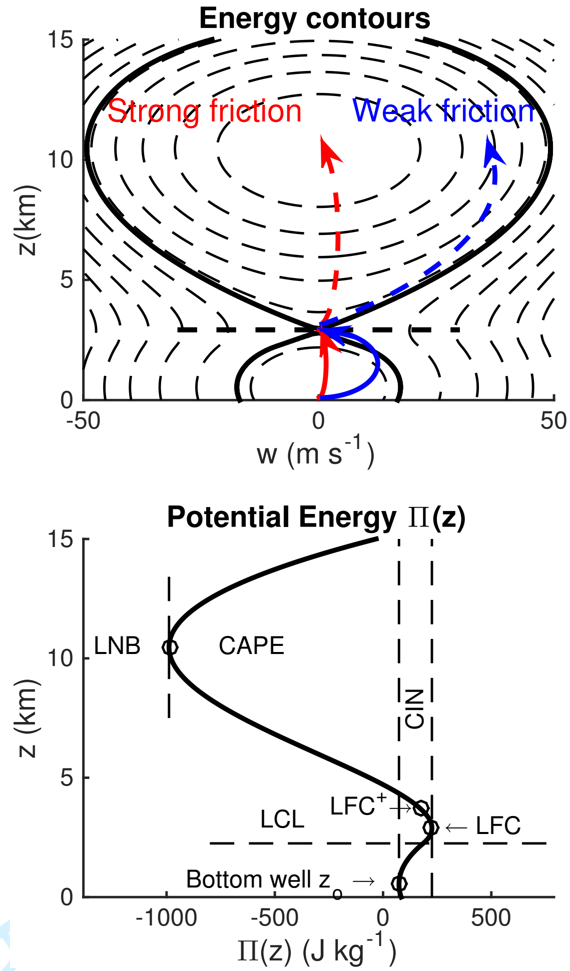

Figure 2. Top: Energy contours (thin solid curve) and separatrix (thick solid curve) $E = E(w=0, z=\text{LFC})$. Red and blue arrows (labeled for the printed version) show an schematic of preferred transition paths for the strong and weak friction regimes respectively (to be explained below). Bottom: Potential energy, showing CIN (CAPE) as the potential energy difference between z_o (LFC) and LFC (LNB). The location of the barrier (LFC$^+$) above in the vicinity of LFC also shown.

implications for the parcel's dynamics when stochastic variability is added, as it is explained in the next sections.

Fig. 2 (top panel) shows contours of the corresponding total energy function, $E(z,w)$. It has three critical points, corresponding to the bottoms of two wells and a saddle point that connects them. The saddle point is an metastable equilibrium point, identified with the level of free convection (LFC). The separatrix here is defined as the curve passing through the saddle point dividing the two wells, and it is plotted with the thick solid line. The separatrix has significance in that it encloses a set of closed contours.

The energy is relevant to the main discussion of the paper—weak and strong friction limits—in the following way. The terms in the parcel model in (2) can be divided into two groups: a deterministic oscillatory component due to buoyancy $(w\,dt, b\,dt)$, and a forced–damped component from the stochastic forcing and mixing of the parcel with its environment $(-wdt/\tau_w + b_w dW)$. When different parameter regimes are explored, one may see the dominance of either of these two components, or possibly both terms equally contributing to the time evolution of the parcels. In particular, we distinguish two main parameter regimes of strong and weak friction. Fig. 2 (top panel) shows an schematic of the observations to be made below with two cartoon arrows on top of the energy contours. It will be seen below that the weak-friction limit corresponds to an evolution that follows an energy contour and has energy conservation, whereas the strong friction limit corresponds to an evolution that crosses energy contours due to frictional effects.

2.3. Parameter calibration

In subsequent sections, the model parameters τ_w and b_w in (2) will take on different values to describe the range of behaviors of the weak- and strong-friction limits. To see the impact of the parameters τ_w and b_w on the behavior of the model, it is useful to consider a simpler version of the model in (2) by neglecting the buoyancy. In that case, w would evolve according to $dw = -(w/\tau_w)\,dt + b_w\,dW$, which is known as the Ornstein–Uhlenbeck process (e.g., Gardiner 2004). This equation involves two components: an exponential decay from the friction, $dw = -(w/\tau_w)\,dt$, plus a random forcing $b_w\,dW$. This equation also arises in other contexts, such as a a particle undergoing Brownian motion under the influence of friction. The values for τ_w and b_w are then seen to be associated with two statistics. First, the covariance of $w(t)$ and $w(s)$ at two times t and s is given by

$$\frac{\tau_w b_w^2}{2}\left(e^{-|t-s|/\tau_w} - e^{-(t+s)/\tau_w}\right) + \mathrm{var}(w(0))e^{-(t+s)/\tau_w}. \tag{13}$$

From this formula, one can see that τ_w describes the decorrelation time. Second, considering a single time $s = t$, in the stationary limit as $s = t \to \infty$, one obtains the stationary variance; its square root is

$$\sigma_w = b_w\sqrt{\tau_w/2}. \tag{14}$$

This is the stationary standard deviation, and it is related to both of the parameters τ_w and b_w. These two statistical quantities can therefore be used for guidance below in selecting and interpreting values of the model parameters b_w and τ_w.

3. Pathways through w–z phase space

In order to illustrate the parcel dynamics in the weak-friction and strong-friction regimes, we first present numerical solutions of (2) using the Euler-Maruyama (EM) method (e.g., Higham 2001). In brief, the Euler-Maruyama method works essentially the same as the commonly used forward Euler method for deterministic differential equations, except a random forcing is also added to represent $dW(t)$. We refer to one "realization" of (2) as the dynamics of $z(t)$ and $w(t)$ that result for one particular sequence of random forcing values ΔW_0, ΔW_1, ΔW_2, $\cdots$, at time steps $t = t_0, t_1, t_2, \cdots$. A different realization is obtained by drawing different random values for ΔW_0, ΔW_1, ΔW_2, $\cdots$. Each value of ΔW_n $(n = 0, 1, 2, \cdots)$ is an independent sample from a Gaussian distribution with mean 0 and variance Δt. Furthermore, by considering an ensemble of many realizations, the probability density can be estimated for the evolution of the parcel.

Fig. 3 shows a case corresponding to weak friction. Here the relaxation timescale is $\tau_w = 7.5\,\mathrm{min}$, which is comparable to the value used in Neggers *et al.* (2002). The noise amplitude is $b_w = 4.91\times10^{-1}\ \mathrm{ms}^{-1}\ \mathrm{s}^{-1/2}$. Under an Ornstein-Uhlenbeck process, as mentioned above in section 2.3, such parameters would have a quasi-stationary standard deviation of $\sigma_w = 7.37\ \mathrm{m\ s}^{-1}$, which is consistent with typical fluctuations of the parcel while in the lower well. The top panel of Fig. 3 shows part of the picture of the evolution of one realization of the parcel from 0 to 5 hours. After first spending considerable time fluctuating in the lower well, the parcel eventually escapes. On its approach toward the upper well, the parcel does not move directly toward the bottom of the well; instead, the parcel ascends along the separatrix with total energy approximately conserved.

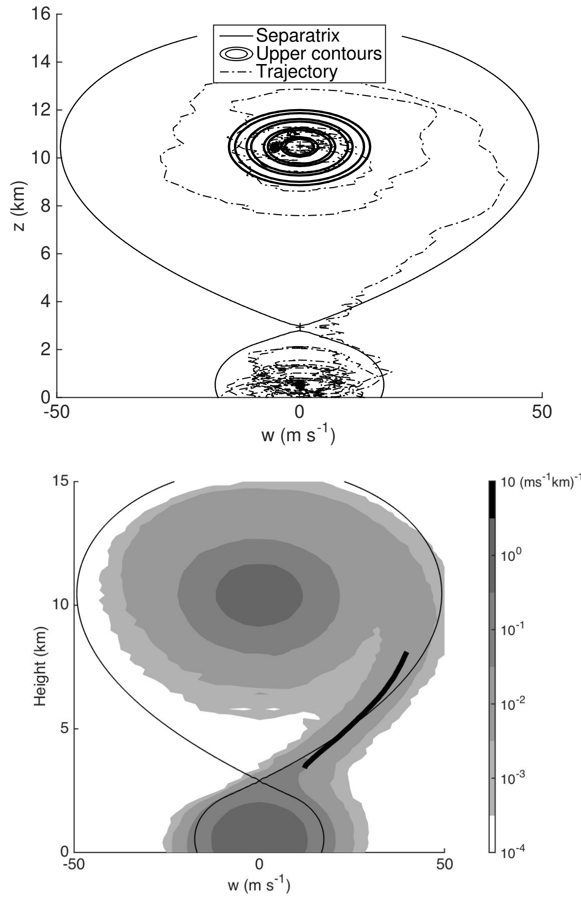

Figure 3. Top: A parcel realization given by equation (2). Also included are the separatrix (thin solid line) and energy contours near the upper well (thick solid lines). Here the noise's amplitude is $b_w = 4.91\times10^{-1}\ \mathrm{ms}^{-1}\ \mathrm{s}^{-1/2}$, the relaxation timescale is $\tau_w = 7.5\,\mathrm{min}$ and the ending time is 5 h. Bottom: Contours of the probability density function (p.d.f.) in the (z, w) plane, in logarithmic scale. Also included is the separatrix (thin solid line)

While the top panel of Fig. 3 shows only one realization, one can see the statistics of preferred paths by analyzing a probability density function (p.d.f.). We obtain an approximation of p.d.f.'s by proceeding with 1000 simulations and accounting for the incidence of a parcel in a bin in the (z, w) plane. The p.d.f.'s are in units of $(\mathrm{ms}^{-1}\ \mathrm{km})^{-1}$ and normalized with respect to the L^1 norm. The first thing to note about the p.d.f., shown in the bottom panel of Fig. 3, is that the most probable state is, by far, the location of the bottom of the lower well, near $w = 0$ and $z = 0.5$ km. This indicates that the convective initiation time is long, and the parcel stays near the bottom well for a long time. As a result, contours of the p.d.f. in other regions of phase space might be hard to visualize, so a logarithmic scale is used for the contours of the p.d.f. We also show a mean path in the following sense. A target height $z = 8$ km is chosen. For each realization we verify whether or not the parcel reaches that height in less than 5 h (the duration of the simulations). If so, we compute the instant of time when the parcel reaches the target and save the path in the (z, w) plane for the previous $15\,\mathrm{min}$. We average over all paths that reached that target. The darker shades indicate the preferred path and aligns with the averaged path. We note that the parcel first accelerates and ascends following a curve close to an energy contour. In a sense, the deterministic component of the system dominates in this case with weak friction.

The statistically preferred path can be quite different depending on various aspects such as environmental profiles and mixing

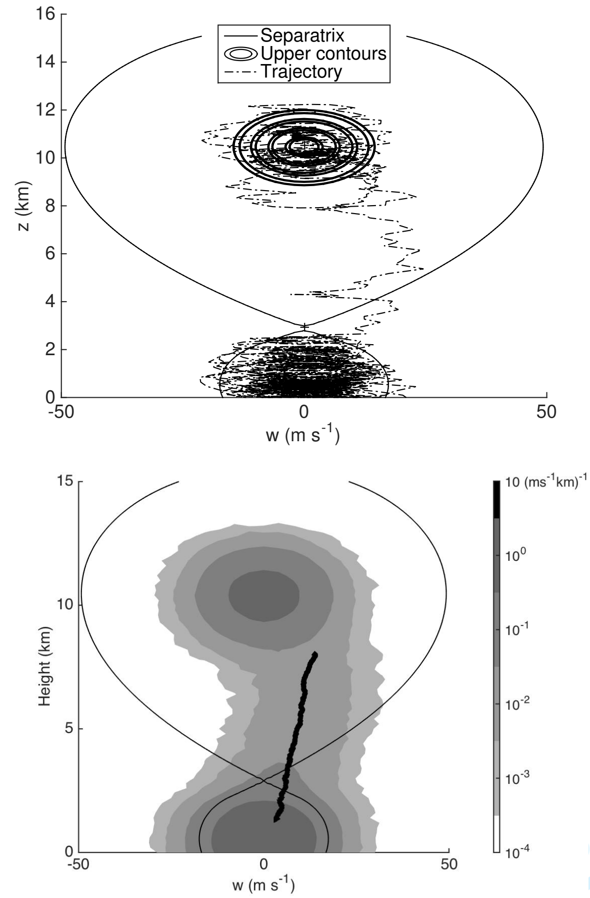

Figure 4. Top: Same as in Fig. 3, with stronger relaxation $\tau_w = 0.75\,\mathrm{min}$ and stronger noise amplitude $b_w = 1.55\mathrm{ms}^{-1}\mathrm{s}^{-1/2}$ in the vertical velocity. Bottom: Contours of the probability density function (p.d.f.) in the (z, w) plane, in logarithmic scale. Also included are the separatrix (thin solid line).

of the parcel with its environment among others. As a second example, the top panel of Fig. 4 repeats the simulation done in Fig. 3 with a stronger friction (smaller τ_w) and noise amplitude in the vertical velocity (larger b_w). The timescale here is $\tau_w = 0.75\,\mathrm{min}$ and the noise coefficient is chosen as $b_w = 1.55\mathrm{ms}^{-1}\mathrm{s}^{-1/2}$. We note that τ_w was reduced by a factor of 10 while b_w was increased by a factor of $\sqrt{10}$ to maintain the same quasi-steady standard deviation $\sigma_w = 7.37\ \mathrm{ms}^{-1}$. In this case, Fig. 4 shows a quite different behavior. Here, when the parcel escapes from the lower well, it transitions to the upper well in a completely different way. Instead of closely following energy contours, the parcel crosses over them and moves almost directly toward the bottom of the upper well. This behavior is indicative of a more significant contribution of the stochastic component and the strong friction.

A schematic summary of Figures 3 and 4 was shown earlier in Fig. 2. In brief, in the weak-friction regime, the parcel appears to rise along a Hamiltonian contour (the separatrix); on the other hand, in the strong-friction regime, the parcel appears to cross Hamiltonian contours as it rises somewhat directly toward the bottom of the upper well. In the strong-friction regime, one could say that the parcel escapes the lower well by moving across the saddle point.

4. Weak- and strong-friction limits

In the previous section, two numerical examples were presented to illustrate the different behavior of parcels in the weak- and strong-friction regimes. In the present section, we seek simplified equations to describe the dynamics in these two limiting regimes. In particular, we show that the weak- and strong-friction limits can be described by reduced equations that arise from asymptotic analysis. Furthermore, a critical friction strength is also identified as the crossover point between the weak- and strong-friction regimes.

4.1. *Weak-friction limit and Hamiltonian system perspective*

In a weak friction regime, one assumes that the friction timescale τ_w is long and the noise amplitude b_w is small. In this limit, the (z, w) system from (2) is a Hamiltonian system:

$$\begin{aligned} \frac{dz}{dt} &= +\frac{\partial E}{\partial w}, \\ \frac{dw}{dt} &= -\frac{\partial E}{\partial z}, \end{aligned} \tag{15}$$

where the energy $E(z, w)$ from (9) plays the role of the Hamiltonian function. In general, Hamiltonian systems are systems of the form $\frac{d}{dt}(p, q) = (\partial H/\partial q, -\partial H/\partial p)$ which are completely determined by a scalar function of position $q = z$ and momentum $p = mw$. The mass m here is assumed constant. For our specific case, the resulting Hamiltonian is $H(p, q) = \frac{p^2}{2m} + m\Pi(q)$. Dividing everything by m, the Hamiltonian system can be rewritten as in (15) with a function of velocity and position $E(z, w)$. Hamiltonian systems have many elegant and illuminating properties, as discussed further below.

Another property of Hamitonian systems is described by Liouville's theorem, which states that the phase space volume of a closed surface is preserved over time. The left panel of Figure 5 shows the evolution of a cloud of 2,000 particles initially located in the region $\left\{(z, w) \middle| \left(\frac{z-1\ \mathrm{km})}{0.5\ \mathrm{km}}\right)^2 + \left(\frac{w-10\ \mathrm{m\,s}^{-1})}{3\ \mathrm{m\,s}^{-1}}\right)^2 \leq 1\right\}$. The initial positions are described by the blue dots while the evolution after 3 min are denoted with light red dots. One can easily observe that the region under the Hamiltonian flow is deformed. The numerically computed area is close to 4.71 km ms^{-1} and remains approximately constant over time (not shown), indicating that the area is preserved. In the second example in this figure (right panel), when the parcels reach the vicinity of the saddle point (i.e., LFC), some parcels continue to ascend, while other parcels descend.

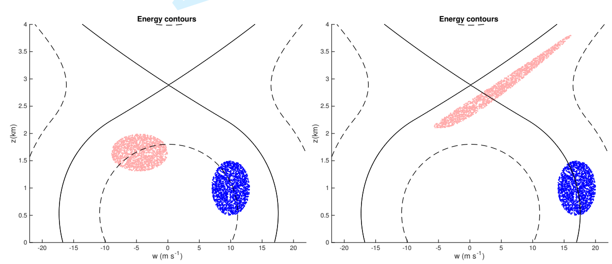

Figure 5. Left panel: Hamiltonian contours as in Figure 2 in the sub-domain $[-22\ \mathrm{ms}^{-1}, 22\ \mathrm{ms}^{-1}] \times [0\ \mathrm{km}, 4\ \mathrm{km}]$, the initial positions of a cloud of 2,000 particles in an ellipse with center at $(z_c = 1\ \mathrm{km}, w_c = 10\ \mathrm{ms}^{-1})$ and radii $z_r = 0.5\ \mathrm{km}$ and $w_r = 3\ \mathrm{ms}^{-1}$ (blue), and their Hamiltonian evolution after 3 minutes (light red). The right panel repeats the previous example where the cloud of particles have center at $(z_c = 1\ \mathrm{km}, w_c = 17\ \mathrm{ms}^{-1})$.

This version of parcel dynamics is commonly used for simple predictions of cloud properties based on adiabatic rising parcel analysis (e.g., Emanuel 1994; Grabowski and Jarecka 2015). For instance, it predicts a maximum vertical velocity of $w_{max} = (2\mathrm{CAPE})^{1/2}$, which arises when all of the potential energy is converted to kinetic energy. These types of model prediction are discussed in more detail in section 5. These simple ideas of energy conversion arise because the model is a Hamiltonian system, and therefore the parcel trajectories preserve total energy and follow the contours in Fig. 2 (top panel).

While it is straightforward to use this Hamiltonian model for a parcel that is rising upward from a starting point at the LFC, it is less straightforward for considering a parcel that begins in the boundary layer (i.e., the lower well) and escapes the lower well and rises into the upper well. For this latter situation, a small amount of (stochastic) forcing is necessary to allow the parcel to escape from the lower well by moving across energy contours. Furthermore, some small amount of friction is needed for the parcel to eventually settle near the LNB, as illustrated earlier in the numerical simulations in Fig. 3.

In summary, in a weak friction regime, we expect a time evolution with the following behavior. A parcel initially located near the bottom well will stay there for a while until some forcing pushes it upward. If the forcing is large enough, the parcel may reach the level of free convection, and it then can escape the lower well and move upward, following a path close to the separatrix. Fig. 2 shows an schematic of such a situation indicated by the blue arrow (labeled for the printed version), and Fig. 3 shows one particular numerical simulation with a small amount of friction and stochastic forcing included. This will be a typical transition from an unsaturated stable parcel to a saturated unstable one in the weak friction regime.

4.2. *Strong friction limit and bistability perspective*

We now look for limiting equations for the case where the friction is asymptotically strong. At the same time, in the original parcel model in (2), we also consider the buoyancy and stochastic forcing to be of similar magnitude to the frictional damping. In this case, it is the acceleration term, dw, that is relatively small; in the limit, it can be set to zero to obtain the relation $wdt = -\tau_w \Pi'(z(t))dt + b_w \tau_w dW$. This is a relation that describes w as a function of z (plus stochastic noise); if it is substituted into the first equation, $dz = w\,dt$, then w can be eliminated from the system to give a limiting equation of

$$dz = -\tau_w \Pi'(z(t))dt + b_w \tau_w dW. \tag{16}$$

Hence the strong-friction limit leads to a stochastic differential equation in terms of only one variable: the height z. We call (16) the strong friction limit of the system (2).

This derivation could be done using systematic asymptotic expansions, as described in more detail in Appendix A. A brief version of the scale analysis is provided next, in order to indicate the precise assumptions that are made in deriving (16).

The scaling assumptions can be summarized by the two small parameters

$$\lambda = \frac{\tau_w}{[t]}, \quad \mu := \frac{[w]^2}{[\Pi]} \tag{17}$$

where $[t]$, $[w]$ and $[\Pi]$ are the time, velocity and potential energy reference scales of the system given by either (45) or (46) in Appendix A, near the lower or upper well, respectively. The strong friction condition reads

$$\mu = O(\lambda), \text{ as } \lambda \to 0. \tag{18}$$

The condition $\lambda << 1$ is directly associated to the strong friction condition. The condition $\mu = O(\lambda)$ says that the potential energy or buoyancy has comparable contribution to the dynamics as the friction.

A bistability viewpoint can be taken for the strong-friction dynamics in (16) by identifying it with the small-mass limit of a particle in a potential well (e.g., Gardiner 2004). The potential

	Small	parameters
	$\lambda = \frac{\tau_w}{[t]}$	$\mu = \frac{[w]^2}{[\Pi]}$
Fig. 3	0.44	0.045
Fig. 4	0.044	0.045

Table 2. Study of parameter regime for Figures 3 and 4. The small parameters λ and μ were obtained according to the scales of the system near the bottom well as in (46).

energy $\Pi(z)$ defines the potential well here, and, as shown in Fig. 2, it is a double-well potential. As a result, the system is bistable in the sense that there are two equilibrium points, one in the lower well (boundary layer) and one in the upper well in the free troposphere (LNB), separated by a saddle point (LFC). If a stochastic forcing can "kick" the parcel high enough, it can potentially move from the lower well to the upper well. This bistability perspective of conditional instability is explored in more detail in section 6 in the context of convective initiation time.

The properties of the strong-friction model in (16) will be described further in section 5, along with comparisons with the properties of the weak-friction model. Before that, we analyze in more detail the assumptions and parameter values that lead to either the weak-friction or strong-friction regime.

4.3. *Analysis of parameter regimes of the numerical results in Section 3*

We are now in a position to analyze the parameter regime of the realizations in Figures 3 and 4. Using the scales defined in equation (46) in Appendix A near the lower or the upper well, Table 2 shows the parameters λ and μ for Figures 3 and 4. The non-dimensional parameter $\lambda = \frac{\tau_w}{[t]}$ is large for Fig. 3 and small for Fig. 4. Regarding the parameter μ associated to the potential energy, it is small and comparable to λ in Fig. 4, which confirms that the parameters used in this figure is in the strong friction regime. For Fig. 3, μ is quite small, but λ is not small and this figure is in a somewhat weak friction regime.

4.4. *Critical friction strength for crossover between weak- and strong-friction regimes*

What is the value of the critical friction strength where the regime changes from weak- to strong-friction above LFC in the upper well? This estimation is obtained now by determining under what conditions we have either oscillatory or decaying solutions in approximate linearized models, similar to damped harmonic oscillators.

To obtain a linearized model, start from the original parcel model in (2) written in terms of z alone as

$$z''(t) + \frac{1}{\tau_w} z'(t) + \Pi'(z(t)) = 0, \tag{19}$$

where the stochastic forcing has been ignored. Near the level of neutral buoyancy, $z \approx$ LNB, the buoyancy force can be linearly approximated as $\Pi'(z) \approx \Pi''(\text{LNB})(z - \text{LNB})$, giving

$$z''(t) + \frac{1}{\tau_w} z'(t) + \Pi''(\text{LNB})(z - \text{LNB}) = 0, \tag{20}$$

which is the equation of a linear damped harmonic oscillator.

This linear model has well-known solution behavior which could either be oscillatory (as in the weak-friction regime) or a non-oscillatory decaying behavior (as in the strong-friction regime). The crossover between oscillatory and decaying behavior occurs for a critical relaxation $\tau_{w,\text{crit}}$ when the discriminant vanishes, and the critical damping parameter is

$$\tau_{w,\text{crit}} = \frac{1}{2\sqrt{\Pi''(\text{LNB})}} \approx \frac{\text{LNB} - \text{LFC}}{2\sqrt{2\text{CAPE}}}. \tag{21}$$

The latter expression arises from a quadratic approximation of the potential energy $\Pi(z)$, and it characterizes the critical damping time scale in terms of the environmental thermodynamic state—in particular, in terms of the LNB, LFC, and CAPE.

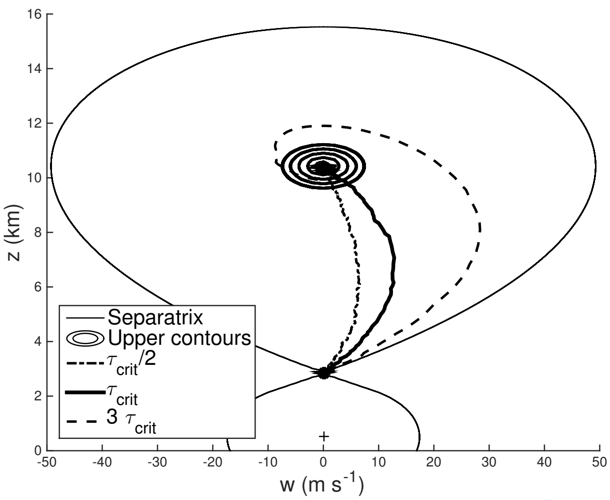

Figure 6. Separatrix (thin solid line), upper contours and parcel's trajectories for $b_w = 4.91 \times 10^{-1}\ \text{ms}^{-1}\ \text{s}^{-1/2}$, and three values of τ_w: $\tau_w = \frac{1}{2}\tau_{w,\text{crit}}$ (dot-dashed line), $\tau_w = \tau_{w,\text{crit}} = 8.94 \times 10^{-1}\text{min}$ (solid line), and $\tau_w = 3\tau_{w,\text{crit}}$ (dashed line).

To illustrate the critical damping rate and the crossover from weak- to strong-friction, Fig. 6 shows three parcel trajectories based on three values of τ_w: $\tau_w = \frac{1}{2}\tau_{w,\text{crit}}$ (dot-dashed line), $\tau_w = \tau_{w,\text{crit}} = 8.94 \times 10^{-1}\text{min}$ (solid line), and $\tau_w = 3\tau_{w,\text{crit}}$ (dashed line). The noise amplitude $b_w = 4.91 \times 10^{-1}\ \text{ms}^{-1}\ \text{s}^{-1/2}$ has been reduced by a factor of 10 compared to the value in Fig. 3. We observe an oscillatory behavior when the relaxation timescale exceeds the critical value. We note that such critical value is based on a linear approximation of Π' around the level of neutral buoyancy in the upper well. Values of τ_w below the critical value could be considered to be in the strong friction regime.

5. Maximum vertical velocity, cloud-top height, and cloud-top time

In this section, we derive and compare several properties of rising parcels in the weak- and strong-friction limits. The properties can all be found analytically, and they can be related to environmental parameters such as CAPE, LNB, etc. Stochastic forcing is not utilized in this section, and the parcel dynamics is initiated at the LFC, similar to common setups of weak-friction parcel ascent. The main new results in this section are the analytical formulas for a parcel's adiabatic ascent in the strong-friction limit. Comparisons between the weak- and strong-friction limits are summarized at the end of the section.

5.1. *Vertical velocity profile*

In the weak friction limit, a parcel's properties can be found by analyzing a Hamiltonian contour, which is the path of the parcel through $z-w$ space. A Hamiltonian contour is described by the equation $E = w^2/2 + \Pi(z)$. If the parcel follows the separatrix, it has conserved energy $E_o = \Pi(\text{LFC})$ (since the parcel initially

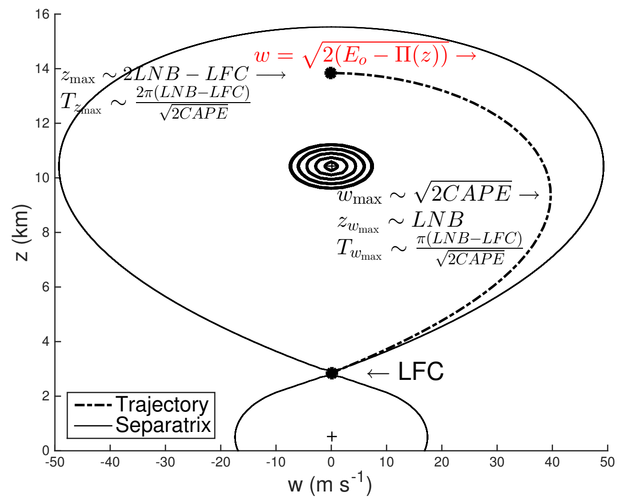

Figure 7. Separatrix, upper contours and parcel's trajectory for the data in Fig. 3 with $b_w = 0$. Also show are the cloud-top height, maximum velocity and the corresponding location and time it takes to get there.

has zero vertical velocity at its initial location of $z \approx \text{LFC}$). Furthermore, one could solve $E = w^2/2 + \Pi(z)$ for w to find the vertical velocity of the parcel as a function of height:

$$w = w(z) = \sqrt{2(E_o - \Pi(z))}. \tag{22}$$

In this case, the maximum vertical velocity occurs at the height of the upper well, $z = \text{LNB}$, and it is

$$w_{\max} = \sqrt{2\text{CAPE}} \quad \text{at} \quad z = \text{LNB}. \tag{23}$$

These properties are summarized in Fig. 7.

To assess the accuracy of these weak-friction approximations, Fig. 7 shows the separatrix and one parcel's trajectory. The maximum vertical velocity predicted by (23) is $49.28\ \text{ms}^{-1}$, compared to a value of $40.18\ \text{ms}^{-1}$ for the example parcel trajectory. The height where this maximum occurs is $z = 9.38$ km, compared to the approximation $\text{LNB} = 10.43$ km.

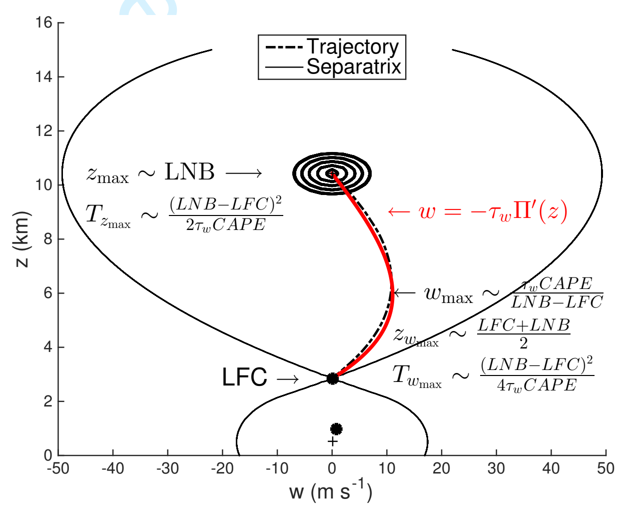

Figure 8. Separatrix, upper contours and parcel's trajectory for the data in Fig. 4 with $b_w = 0$. The graph of $w = -\tau_w \Pi'(z)$ is plotted in a red solid line. Also show are the cloud-top height, maximum velocity and the corresponding location and time it takes to get there.

In the strong friction limit, on the other hand, a parcel rises according to the balance relation

$$w = w(z) = -\tau_w \Pi'(z), \tag{24}$$

which arose above (16) in the derivation of the strong-friction limiting dynamics, and stochastic forcing has been ignored here. This equation describes the parcel's vertical velocity as a function of height, with a maximum velocity

$$w_{\max} = \max_{\mathrm{LFC} \le z \le \mathrm{LNB}} -\tau_w \Pi'(z) \sim \frac{\tau_w \mathrm{CAPE}}{\mathrm{LNB} - \mathrm{LFC}}, \qquad (25)$$

where this maximum vertical velocity is achieved at a height of (LFC+LNB)/2, the average of the LFC and LNB. These properties are summarized in Fig. 8.

To assess the accuracy of these strong-friction approximations, Fig. 8 shows one parcel's trajectory on top of the profile (25). A very good agreement is seen between the two profiles. The maximum vertical velocity and the corresponding height predicted by (25) are $11.05\ \mathrm{ms}^{-1}$ and 5.96 km respectively. On the other hand, the values for the example trajectory shown are $11.49\ \mathrm{ms}^{-1}$ and 7.44 km respectively.

5.2. *Cloud-top height*

For interpreting the parcel model, we use the term cloud-top height for the maximum height achieved by the rising parcel.

In the weak friction limit, the cloud top height according to (22) is approximated as

$$z = \Pi^{-1}(E_o) \sim \mathrm{LFC} + 2(\mathrm{LNB} - \mathrm{LFC}) = 2\mathrm{LNB} - \mathrm{LFC}, \quad (26)$$

where the inverse is taken for $z > \mathrm{LFC}$. For the parameter values used here, the estimated cloud-top height in equation (26) is roughly near $z = 15$ km, and, for comparison, the parcel's maximum height in the example trajectory in Fig. 7 is 13.85 km.

In the strong friction limit, on the other hand, the profile in (24) shows us that the cloud top height can be approximated as

$$z = \mathrm{LNB}, \qquad (27)$$

where the LNB here is $z = \mathrm{LNB} = 10.43$ km. For comparison, for the example trajectory in Fig. 8, the maximum height is 10.63 km.

5.3. *Cloud-top time*

We use the term "cloud-top time" to refer to the time taken for a parcel to rise from the LFC to its maximum height.

In the weak-friction regime, a simple approximation of the cloud-top time can be found through an approximation of the Hamiltonian dynamics. In particular, if the potential energy $\Pi(z)$ can be approximated by a quadratic function, then the dynamics is

$$\frac{d^2 z}{dt^2} \approx -\Pi''(\mathrm{LNB})(z - \mathrm{LNB}), \qquad (28)$$

which is the equation for a simple harmonic oscillator, with oscillation period of $2\pi/[\Pi''(\mathrm{LNB})]^{1/2}$. Under this approximation, the parcel reaches its top height at about half the period, which is

$$T(z_o \to c) \approx \frac{\pi}{\sqrt{\Pi''(\mathrm{LNB})}} \sim \frac{\pi(\mathrm{LNB} - \mathrm{LFC})}{\sqrt{2\mathrm{CAPE}}}, \qquad (29)$$

where c is the cloud top height.

In the strong friction regime, on the other hand, we use the limiting equation (16). Here, a simple approximation of the cloud-top time can also be found if the potential energy $\Pi(z)$ is approximated by a quadratic function, in which case the dynamics is

$$dz \approx -\tau_w \Pi''(\mathrm{LNB})(z - \mathrm{LNB})dt + b_w \tau_w dW, \qquad (30)$$

which is an Ornstein-Uhlenbeck process. The mean trajectory of this approximated process has an analytical formula of

$$\bar{z}(t) = \mathrm{LNB} - (\mathrm{LNB} - z_o)\exp\left(-\tau_w \Pi''(\mathrm{LNB})t\right). \qquad (31)$$

Here the initial position of the parcel is located at the level of free convection. Notice that, in the current approximation, the cloud top height is identified with the level of neutral buoyancy and the mean will take an infinite amount of time to reach it; therefore, we compute the time it takes to get very close to the LNB—e.g., to 90%, 95%, or 98% of the height of the LNB, as illustrated in Fig. 9. Since the distance from LFC to the cloud top height is LNB − LFC, the time it takes to cover a factor r of the target is

$$T(\mathrm{LFC} \to \mathrm{LNB}) = \frac{-\log(1-r)}{\tau_w \Pi''(\mathrm{LNB})} \sim \frac{(\mathrm{LNB} - \mathrm{LFC})^2}{2\tau_w \mathrm{CAPE}}. \qquad (32)$$

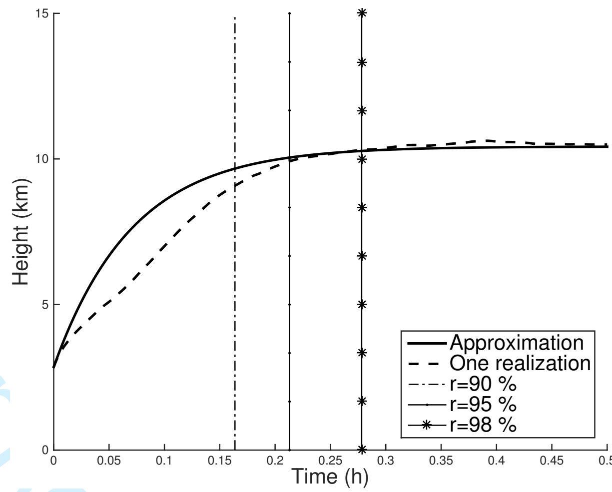

Figure 9. Height versus time for one example trajectory with the parameter values used in Fig. 4 (dashed line) and the mean height predicted by (31). The vertical lines predict the time to reach 90%, 95% and 98% of the target.

Fig. 9 shows the height versus time for a parcel realization (dashed line) and compares it with the approximation in (31) (solid line), showing a good qualitative agreement. The vertical lines denote the time it takes to reach 90%, 95% and 98% of the target, which is the LNB. One can also observe a good agreement between the time it takes to get close to the LNB and the predictions.

5.4. *Summary and comparisons*

The weak- and strong-friction limits were seen above to have distinctly different properties, and one could argue that some of the properties in the strong-friction limit are actually more realistic. In particular, in the weak-friction limit (Fig. 7), the parcel rises far above the LNB, and it actually attains its maximum vertical velocity at the LNB. Such behavior is arguably unrealistic, since the LNB is typically regarded as an estimate of cloud top, and since maximum vertical velocities are typically attained below the LNB or cloud top (e.g., Takahashi and Luo 2012, 2014; Takahashi *et al.* 2017). These discrepancies could be regarded as due to the absence of interactions between the parcel and its environment in the traditional (weak-friction) parcel model. On the other hand, in the strong-friction limit (Fig. 8), the parcel's momentum is damped through interaction with the environment. In this limit, the parcel's behavior is arguably more realistic: the parcel attains its maximum height at the LNB and its maximum vertical velocity about half-way between the LFC and LNB. This suggests that the strong-friction limit provides, at the least, an interesting opposing bound on convective properties compared to the traditional weak-friction limit, and it possibly even provides a more realistic version of parcel theory.

6. Convective initiation time and analytic approximations

Another useful quantity to estimate is the convective initiation time—i.e., the time elapsed in waiting for a parcel to rise from the boundary layer to a barrier located above in the vicinity of LFC, at which point convection will initiate. The convective initiation time should be a random quantity, since it should depend on the essentially random fluctuations of boundary layer turbulence that eventually provide the "kick" necessary to lift the parcel to the LFC. To model such a random process, we use the stochastic version of the parcel model shown in (2).

In what follows in this section, an analytical approximation is derived for the convective initiation time, providing yet another fundamental quantity that can be derived from parcel theory. Numerical simulations are also presented in order to illustrate the error involved in the analytical approximation. It is also noteworthy that the analytical approximation arises from using the strong-friction limit of parcel theory.

6.1. Analytic approximation of the convective initiation time

The convective initiation time problem can be viewed as a bistability problem. In more detail, and to define notation, note that the system is endowed with a double well potential (see Fig. 2) with two stable equilibrium points, z_o and the LNB, and one unstable equilibrium point, the LFC. Initially, the parcel is located in the boundary layer near z_o, and if it can rise to the LFC, then it will transition to the deeper (upper) well. Therefore, it is sufficient to place an absorbing barrier LFC$^+$ above in the vicinity of LFC and to examine the time required to reach LFC$^+$ (see Fig. 2 to see its location). The mean convective initiation time from z_o to LFC$^+$ is denoted as $T(z_o \to \text{LFC}^+)$. We can then analyze $T(z_o \to \text{LFC}^+)$ from the point of view of an *escape problem from a double well potential*.

In this situation, for the strong-friction dynamics in (16), the mean convective initiation time is approximately

$$T(z_o \to \text{LFC}^+) \sim T_o = 2\pi\sqrt{\frac{-1}{U''(\text{LFC})}}\sqrt{\frac{1}{U''(z_o)}}\exp\left(\frac{2|\text{CIN}|}{b_w^2\tau_w}\right). \tag{33}$$

This formula is the classical Arrhenius formula (e.g., Gardiner 2004), and the derivation is described in Appendix B. This approximation of $T(z_o \to \text{LFC}^+)$ holds in an asymptotic limit as

$$\mu = \frac{b_w^2\tau_w}{2|\text{CIN}|} \to 0. \tag{34}$$

Strictly speaking, it means that the relative error, which is a non-dimensional quantity, satisfies

$$\frac{T - T_o}{T_o} = O(\mu), \text{ as } \mu \to 0, \tag{35}$$

where T depends on μ and T_o is the limiting value for $\mu \to 0$. In fact, we can compute the second term in the asymptotic expansion as

$$\frac{T - T_o}{T_o} = \left(\frac{1}{8}\frac{U^{(4)}(\text{LFC})}{(U''(\text{LFC}))^2} - \frac{1}{8}\frac{U^{(4)}(z_o)}{(U''(z_o))^2} - \frac{5}{24}\frac{(U'''(\text{LFC}))^2}{(U''(\text{LFC}))^3} + \frac{5}{24}\frac{(U'''(z_o))^2}{(U''(z_o))^3}\right)\frac{b_w^2\tau_w^2}{2} + O(\mu)^2. \tag{36}$$

	Small	parameters
	$\lambda = \frac{\tau_w}{[t]}$	$\mu = \frac{[w]^2}{[\Pi]}$
Fig. 3	1.41	0.36
Fig. 4	0.14	0.36

Table 3. Study of parameter regime for Figures 3 and 4. The small parameters λ and μ were obtained according to the scales of the system near the bottom well as in (45).

This small parameter μ is the same one that is described in (17) and Appendix A. Physically, a small value of μ could correspond to relatively strong CIN and/or relatively strong friction (small τ_w), and a consequence of this scenario is a relatively long time until convection is initiated.

The formula in (33) is potentially valuable because it describes a quantity of interest (convective initiation time) in terms of environmental parameters, as well as friction rate and turbulent intensity. In this sense, it provides yet another simple prediction, in addition to the quantities described above in section 5 (maximum vertical velocity, cloud-top height, etc.), provided by parcel models.

6.2. Numerical illustration for the strong friction limit

To illustrate the asymptotic approximation in (33), Fig. 10 shows the $(t, z(t))$ trajectory for one parcel realization that escapes the bottom well, a vertical line located at the convective initiation time ("-+") and a vertical line located at the approximated convective initiation time (33). The evolution of height with respect to time is obtained using the limiting equations (16) and the parameter values used in Figures 3 and 4. That is, $\tau_w = 7.5\text{min}, b_w = 4.91 \times 10^{-1}\ \text{ms}^{-1}\ \text{s}^{-1/2}$ for the top panel and $\tau_w = 0.75\text{min}, b_w = 1.55\text{ms}^{-1}\text{s}^{-1/2}$ for the bottom panel. The convective initiation time is computed using a Monte-Carlo approach with 5000 realizations. The two vertical lines are close to each other in both cases, which indicates that the approximation in (33) is accurate.

The values of λ and μ for this case are summarized in Table 3. The values are calculated using the scales near the bottom well in equation (45) in Appendix A. One can observe a reasonably small value of μ in both cases. On the other hand, the parameter λ is small only in the case of Fig. 4 (so also Fig. 10 bottom). Hence the parameter values for Fig. 10, top panel, are in the weak friction regime, while those used in Fig. 10, bottom panel, correspond to the strong friction regime for the bottom well.

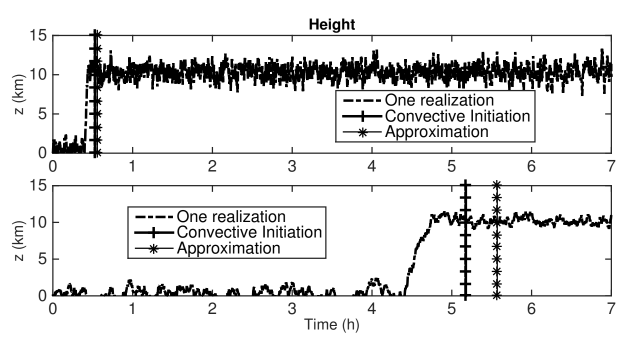

Figure 10. Convective initiation time for the values in Figures 3 (top) and 4 (bottom). In each panel one realization computed with the limiting equations (16) is shown. The vertical line with plus signs indicate the mean convective initiation time statistically computed using 5000 realizations. The vertical line with '*' signs show the approximation used in (33).

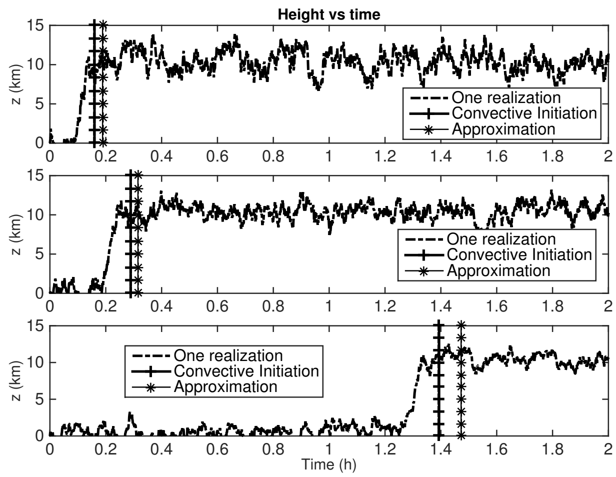

Figure 11. One example realization (dashed line), numerical mean convective initiation time (vertical "-+" line) and the approximated mean convective initiation time in equation (33) (vertical "-*" line). The relaxation timescale is $\tau_w = 3.75$min. The noise coefficients are given by $b_w = 1.15\text{ms}^{-1}\text{s}^{-1/2}$ (top panel), $b_w = 0.936\text{ms}^{-1}\text{s}^{-1/2}$ (middle panel) and $b_w = 0.663\text{ms}^{-1}\text{s}^{-1/2}$ (bottom panel).

	Error	analysis			
Fig. 11	μ	T_o	$\lvert T-T_o\rvert$	$\frac{\lvert T-T_o\rvert}{T_o}$	$\frac{\lvert T-T_o\rvert}{T_o\mu}$
Top	0.97	0.19 h	1.74 min	0.15	0.16
Middle	0.65	0.32 h	1.57 min	0.08	0.13
Bottom	0.32	1.47 h	4.72 min	0.05	0.16
Fig. 10					
Top	0.36	0.56 h	1.72 min	0.05	0.14
Bottom	0.36	5.57 h	23.62 min	0.07	0.20

Table 4. Small parameter μ (first column), relative error (second column) and its ratio (third column). The small parameter was obtained according to the scales of the system near the bottom well given by (45).

6.3. *Error analysis and other parameter values*

To analyze the error involved in the asymptotic approximation, we consider a sequence of test cases for different values of the parameter b_w. In this parameter study, we consider different values from those used in Fig. 10. In all cases, the relaxation timescale is fixed at $\tau_w = 3.75$min. In each panel of Fig. 11, we show one example realization (dashed black line) for the particular value of the parameter b_w used in that panel. In descending order, Fig. 11 shows the results for $b_w = 1.15\text{ms}^{-1}\text{s}^{-1/2}$ (top panel), $b_w = 0.936\text{ms}^{-1}\text{s}^{-1/2}$ (middle panel) and $b_w = 0.663\text{ms}^{-1}\text{s}^{-1/2}$ (bottom panel). Such values correspond to correlation amplitudes of $\sigma_w = 12.17\ \text{ms}^{-1}, 9.94\ \text{ms}^{-1}$ and $7.03\ \text{ms}^{-1}$ respectively. In addition, two vertical lines are included, one corresponding to the approximated convective initiation time ('-*') and the other denoting the convective initiation time computed using a Monte-Carlo approach with 5000 simulations. The numerical mean value and the asymptotic mean value are seen to be close to each other, which indicates that the asymptotic mean value is a reasonably accurate approximation.

Table 4 shows the error in the approximation T_o of the convective initiation time $T(z_o \to \text{LFC}^+)$. Both the absolute and relative error are shown to clarify the behavior as μ becomes smaller. In particular, there appears to be the largest error for the smallest value of μ, based on the bottom panel of Fig. 11, in comparison to the other panels that have larger μ values. This is somewhat counterintuitive since one expects smaller error as μ becomes smaller, and the explanation is that it is the relative error rather than the absolute error that becomes smaller as μ becomes smaller. See (35) which shows this fact, since the convective initiation time T itself is a growing function of μ as $\mu \to 0$. In fact, the relative error $|T - T_o|/T_o = O(\mu)$ decreases linearly with respect to μ according to equation (35), as shown in the last column of the table.

μ	3.24×10^{-1}	3.24×10^{-2}	3.24×10^{-3}
Rel. error	2.6×10^{-2}	1.0×10^{-3}	0.98×10^{-4}
Eq. (36)	1.0×10^{-2}	1.0×10^{-3}	1.02×10^{-4}

Table 5. Second term in the expansion. The parameter μ (first row), relative error (second row) and the second term in the asymptotic expansion of the convective initiation time given by equation (36) (third row) are shown. The parameter values taken from the bottom panel of Fig. 11 ($b_w = 0.663\text{ms}^{-1}\text{s}^{-1/2}$) were used to compute the corresponding values in the first column of this table. The rest of the columns take reduced values of b_w to reduce μ by factors of 10 and 100 in columns 2 and 3 respectively.

For the sake of completeness, we include the corresponding calculations in Table 4 for the parameter values used in Fig. 10. We note that $\mu = 0.36$ for both panels, even when τ_w and b_w are different in both cases. However, the convective initiation time for the bottom panel is almost 10 times the convective initiation time of the top panel. In any case, the ratios $|T - T_o|/(T_o\mu)$ are not too far from each other.

The second term in the asymptotic expansion of the convective initiation time (36) is verified in Table 5. The small parameter μ is specified in the first row, the relative error $|T - T_o|/T_o$ is shown in the second row and the last row displays the value of the second term in the expansion, given by the right hand side of equation (36). In the first column, we take the parameter values used in the bottom panel of Fig. 11. The rest of the columns take reduced values of b_w to reduce μ by a factor of 10 with respect to the previous column. We note that the convective initiation time grows exponentially when $\mu \to 0$, and it is quite large for the second and third columns, which are included here mainly to verify the second term in the expansion. Calculating $T(z_o \to \text{LFC}^+)$ with the Monte Carlo approach is not possible in practice for these cases. Instead, we compute the exact T given by equation (51). We note that for small enough values of μ, a very good agreement between the relative error and the second term in the expansion is observed.

6.4. *Distribution of escaping times*

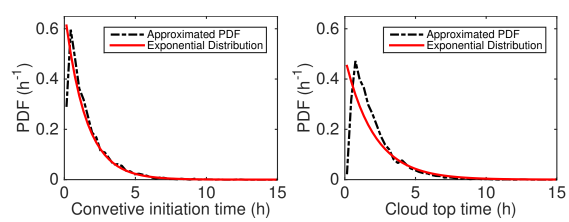

Figure 12. Probability density function of the time where the parcel reaches the absorbing barrier $z = \text{LFC}^+ = 3.43$ km (left), starting in the lower well ($z = 0.5$ km), averaged over an ensemble of 5000 realizations. The red solid curve denotes the exponential distribution in equation (37). Here the parameter values were taken from the bottom panel of Fig. 11 ($b_w = 0.663\text{ms}^{-1}\text{s}^{-1/2}$ and $\tau_w = 3.75$min), which gives $T_o = 1.47$ h. The right panel repeats the graph for the barrier $z = 12$ km (right) and T_o is replaces by $T_1 = 2.06$ h.

Beyond the mean value, one can seek further details by analyzing the distribution of escaping times. Fig. 12 (left panel) shows a p.d.f. of the time where the parcel reaches the absorbing barrier located at $z = \text{LFC}^+ = 3.43$ km, which is 0.5 km above the level of free convection (top) and $z = 12$ km (bottom), starting in the lower well ($z = 0.5$ km), averaged over an ensemble of 5000 realizations. The parameter values for this p.d.f. were taken from Fig. 11 (bottom panel). The red curve shows the exponential distribution with mean T_o, given by

$$\rho(t) = \frac{1}{T_o} e^{-t/T_o} H(t), \tag{37}$$

where H is the Heaviside function. One can observe a very good agreement between the p.d.f. and the red curve, giving evidence that the distribution of escaping times is exponential with mean convective initiation time, approximated by T_o. The right panel considers the time needed for the parcel to reach a higher altitude, as an estimate of the time needed to reach cloud top. Replacing the mean T_o by the mean of the cloud top time $T_1 = 2.06$h, we also observe an exponential distribution.

These results suggest that the convective initiation time could be modeled (e.g., as part of a convective trigger in a convective parameterization) as a random variable with an exponential distribution. The exponential distribution is a one-parameter distribution, where the one parameter can be taken to be the mean, which here could be specified using the asymptotic formula in (33).

6.5. *Validation of the convective initiation time in the full system*

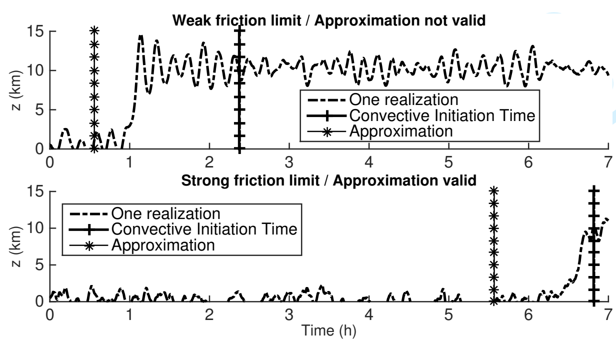

Figure 13. Top: Convective initiation time for the values in Fig. 3 using the full system. Bottom: Convective initiation time for the values in Fig. 4 using the full system.

The earlier parts of this section were based on the strong-friction limiting dynamics in (16) as the starting point, from which the asymptotic approximation in (33) was derived. Now we go back one step further and compare the asymptotic approximation with the full system in (2). One expects the asymptotic approximation to describe the full system in (2) when both λ and μ are small—i.e., when the full system is in the strong-friction regime. Some test cases are now described to compare with the full system for some different values of λ and μ that are small or not too small.

Fig. 13 shows a realization $(t, z(t))$ for the full system (2), the numerically computed mean convective initiation time (line "+") obtained with a Monte-Carlo approach using 5000 realizations and the corresponding approximation (33) (line "-*"). The top panel uses the parameter values in Fig. 3: $\mu = 0.36$ and $\lambda = 1.41$ (see Table 3). The relative error $|T - T_o|/T_o$ is 3.26, which is quite large. This is consistent with the fact that the full system is not in the strong friction regime and as a consequence the approximation (33) is not accurate. On the other hand, the bottom panel shows the corresponding quantities for the parameter values used in Fig. 4, which are closer to the strong friction regime: $\mu = 0.36$ and $\lambda = 0.14$ (see Table 3). Even though the buoyancy term parameter $\mu = 0.36$ is not too small, the approximation (33) is still valid for the full system in this case. This can be corroborated with the relative error, which is 0.22 in this case.

7. Discussion

7.1. *Alternative parameterizations of friction*

In the text above, the friction was assumed to take the linear-in-w form of $\tau_w^{-1} w$ in order to simplify some calculations, but other choices of the friction could be used to obtain similar results. For instance, it is common to use frictional damping that is quadratic in w (e.g., Simpson and Wiggert 1969; Jakob and Siebesma 2003; Brast *et al.* 2016), which leads to a vertical velocity equation of the form

$$\frac{dw}{dt} = -\epsilon_{ent}(z)|w|w + b(z), \tag{38}$$

where $\epsilon_{ent}(z)$ is the entrainment coefficient. (Note that we write the drag as $|w|w$ so it decelerates a parcel that is either rising or falling; it is more commonly written as w^2 in the literature in contexts where the parcel is assumed instead to be always rising.)

In the strong-friction limit, (38) would become

$$\lambda_{ent}|w|w = b(z), \tag{39}$$

or, upon solving for w,

$$\frac{dz}{dt} = \text{sgn}[b(z)]\sqrt{\frac{|b(z)|}{\epsilon_{ent}(z)}}, \tag{40}$$

where $w = dz/dt$ was used to arrive at an equation for $z(t)$ alone. Also used to arrive at (40) is the relation $\text{sgn}(w) = \text{sgn}[b(z)]$, deduced from (39), where sgn is the sign function. The result in (40) is the quadratic-in-w analog to the linear-in-w dynamics of (16), and the main difference is the square root. For the quadratic-in-w case, similar results could be obtained for the bistability perspective, convective initiation time, etc.

7.2. *Entrainment of moisture and equivalent potential temperature*

Adiabatic parcel dynamics have been assumed here, where the values of q_t and θ_e are conserved, in the main results of the paper. It would be interesting in the future to investigate non-adiabatic cases with entrainment of moisture and equivalent potential temperature in which case the dynamics of the parcel's thermodynamic variables could be modeled as

$$\frac{d\theta_e}{dt} = -\frac{1}{\tau_\theta}(\theta_e - \theta_{e,env}(z)), \tag{41a}$$

$$\frac{dq_t}{dt} = -\frac{1}{\tau_q}(q_t - q_{t,env}(z)), \tag{41b}$$

where entrainment would relax the parcel's θ_e and q_t values toward their environmental values of $\theta_{e,env}$ and $q_{t,env}$, and where a constant entrainment coefficient has been written for illustrative purposes but could be replaced by a more sophisticated parameterization without causing any major change to the discussion.

Three limits are possible for (41). First, if the entrainment is weak, then the adiabatic case is obtained, as used here in the main results of the paper. Second, if the entrainment is strong, then the parcel's θ_e and q_t values are rapidly relaxed toward the environmental values of $\theta_{e,env}(z)$ and $q_{t,env}(z)$, so that $\theta_e \approx \theta_{e,env}(z)$ and $q_t \approx q_{t,env}(z)$; this case would perhaps be uninteresting since the buoyancy would be small or zero. Third, if the entrainment is $O(1)$, then the evolution of θ_e and q_t must be retained, with entrainment, as in (41).

While the third case is more complicated, the first case (the adiabatic case) allows a very convenient simplification: the dynamics is a gradient system. This means that the dynamics can be written as $dz/dt = dF/dz$, where $F(z)$ is a function of z. In this case, some quantities such as convective initiation time can be found analytically, as shown above. On the other hand, in the third case where entrainment is $O(1)$ and θ_e and q_t are evolving as in (41), the dynamics are a nongradient system. This means that the dynamics do not take the form $dz/dt = \partial F/\partial z$, $d\theta_e/dt = \partial F/\partial \theta_e$, $dq_t/dt = \partial F/\partial q_t$ for some function $F(z, \theta_e, q_t)$. In such a case, it is more difficult and sometimes unknown how to obtain analytical formulas for quantities such as convective initiation time (Bouchet and Reygner 2016; Tao 2018). It would be interesting to further investigate this case in the future. Moreover, it would also be interesting, following the ideas of transition path theory (Metzner *et al.* 2006), to study not only the *time* to initiate convection but also the *pathway* taken in the transition.

7.3. *Effects of comprehensive thermodynamics*

In the text above, we used simplified thermodynamics, such as the linearized formulas for θ_e and θ_v in (6), since it allows analytical formulas to be obtained. However, we have also considered cases with comprehensive thermodynamics, and the main results of this paper are essentially the same, although some of the results can only be determined numerically, not analytically.

8. Conclusions

The weak- and strong-friction limits of a parcel model were investigated here as limiting cases of the vertical velocity equation

$$\frac{dw}{dt} = b(z) - \Gamma(w, z), \tag{42}$$

along with $dz/dt = w$, where $b(z)$ is the buoyancy and $\Gamma(w, z)$ is the momentum drag or friction. The weak-friction limit is the traditional limit

$$\frac{dw}{dt} = b(z), \tag{43}$$

which arises when the drag $\Gamma(w, z)$ is small. In this limit, the dynamics of z and w is a Hamiltonian system. The strong-friction limit, on the other hand, is given by

$$\frac{1}{\tau_w}\frac{dz}{dt} = b(z) + f, \tag{44}$$

which was derived here under the assumption of small acceleration dw/dt relative to friction and buoyancy. [In writing (44), it was assumed that the friction has the simple form $\Gamma(w, z) = \tau_w^{-1} w$; alternative forms of $\Gamma(w, z)$ were discussed in section 7.1 and lead to similar equations.] In brief, the key observation is that there are essentially two important time scales: the frictional time scale and the buoyancy time scale.

As one main result, the strong-friction limit may provide a more accurate estimate of cloud-top height. In particular, the strong-friction limit predicts that the cloud-top height will be the LNB, whereas the weak-friction limit predicts that the cloud-top height will be approximately *twice as high* as the LNB. While more realistic estimates of cloud-top height can also be obtained by including entrainment of environmental moisture, the value of the strong-friction, adiabatic model is that it can be solved exactly and provides analytical formulas. For example, the parcel's vertical velocity is predicted to be $w(z) \approx \tau_w (g/\theta_0)\theta_v'(z)$, which is proportional to the friction time scale τ_w and the buoyancy; the parcel reaches its maximum vertical velocity in the mid-troposphere and its vertical velocity decreases toward zero as it approaches the LNB.

A potential practical use is to stochastic convective parameterizations. In particular, a stochastic trigger could be formulated based on the strong-friction limit. It was seen in section 6 that the convective initiation time is approximately an exponential random variable, and its mean value is given asymptotically by the formula in (33). To determine whether convection should be initiated during a climate model time step Δt, one could draw exponential random variables for the convective initiation time and check to see whether they are less than μt—i.e., whether convection has initiated during the time step.

Acknowledgments

The research of G.H.-D. is partially supported by grant UNAM-DGAPA-PAPIIT IN113019. The research of L.M.S. and S.N.S. is partially supported by grant NSf AGS 1443325. The research of S.N.S. is partially supported by a Sloan Research Fellowship from the Alfred P. Sloan Foundation and a Vilas Associates Award from the University of Wisconsin-Madison.

A. The limiting strong friction dynamics

The goal of this appendix is to present the details in the derivation of the limiting equations for the strong friction regime. For instance, under what conditions on CAPE, CIN, and frictional dissipation rate is the strong-friction limit valid?

A.1. *The scales of the system*

One needs to choose the scales of the system based on the parameters involved in the equations. We note that the parcel's dynamics may exhibit different behavior below and above the level of free convection, so we identify two different sets of scales, one for each well, and given by

$$[\Pi] = |\mathrm{CIN}|, [z] = \mathrm{LFC} - a, [w] = b_w\sqrt{\tfrac{\tau_w}{2}}, [t] = \tfrac{[z]}{[w]} \tag{45}$$

for the lower well and

$$[\Pi] = \mathrm{CAPE}, [z] = \mathrm{LNB} - \mathrm{LFC}, [w] = b_w\sqrt{\tfrac{\tau_w}{2}}, [t] = \tfrac{[z]}{[w]} \tag{46}$$

for the upper well. We note that the velocity scale is of stochastic type in the sense that it is the quasi steady state standard deviation if we were under an Ornstein-Uhlenbeck process. On the other hand, the scale for the potential energy is of deterministic type in the sense that |CIN| and CAPE are related to the depth of the bottom and upper wells and they determine the periods of the parcels if we only consider the Hamiltonian system with no relaxation or stochastic noise. The quantity $\Pi'(z)$ is non-dimensionalized with the scale $[\Pi'] = [\Pi]/[z]$. For the potential energy used in this work, $z_o = 0.5$km, LFC $= 2.85$ km, LNB $=$ 10.43 km, CIN $= 152.18$J kg^{-1} and CAPE $= 1214.2$J kg^{-1}.

We observe that the relaxation timescale τ_w for Figures 3 and 4 differ by a factor of 10, and the corresponding coefficient b_w by a factor of $1/\sqrt{10}$ such that the stationary standard deviation coincide. As a result, the velocity scales are the same for those two parameter values. One could think of other velocity scales such as the maximum velocity given by the separatrix near each well, which would be of deterministic type. We expect that the velocity scale chosen in (45) or (46) is the smaller of the two. For the parameters used in Figures 3 and 4, the velocity scale is $[w] = 7.37$ ms^{-1}. The length scales are given by $[z] = 2.36$ km and $[z] = 7.57$ km for the lower and upper wells, respectively.

A.2. Nondimensional parameters and distinguished limit

To identify the nondimensional parameters μ and λ and how they they are related in the strong-friction limit, it is convenient to work with the Fokker-Planck equation rather than the stochastic differential equation itself. Let $P(z, w)$ be the probability density function of system (2) and let us recall that $b = \frac{g}{\theta_o}\theta_v' = -\Pi'(z)$. The corresponding Fokker-Planck equation is given by

$$\frac{\partial P}{\partial t} = -w\frac{\partial P}{\partial z} + \Pi'(z)\frac{\partial P}{\partial w} + \frac{1}{\tau_w}\frac{\partial (wP)}{\partial w} + \frac{b_w^2}{2}\frac{\partial^2 P}{\partial w^2}. \tag{47}$$

Using the definitions in (17) and the relation $\frac{b_w^2[t]/2}{[w]^2} = \frac{[t]}{\tau_w} = \lambda^{-1}$, the non-dimensional version of equation (47) becomes

$$\frac{\tilde{\partial} P}{\partial \tilde{t}} = -\tilde{w}\frac{\partial \tilde{P}}{\partial \tilde{z}} + \mu^{-1}\tilde{\Pi}'(\tilde{z})\frac{\partial \tilde{P}}{\partial \tilde{w}} + \lambda^{-1}\frac{\partial (\tilde{w}\tilde{P})}{\partial \tilde{w}} + \lambda^{-1}\frac{\partial^2 \tilde{P}}{\partial \tilde{w}^2}. \tag{48}$$

This equation suggests the distinguished limit $\mu = O(\lambda)$, as presented in the main text in (18), in order to have comparable strength of the terms for friction, stochastic noise, and buoyancy (Π').

B. Asymptotic analysis for the mean convective initiation time

The topic of this appendix is a simplified formula for the average convective initiation time, in an asymptotic limit for strong friction regime. In particular, in the derivation here, the connection is described with the two small parameters λ and μ of the strong-friction limit, and the error term is presented explicitly.

To simplify notation, it is convenient to define the potential U and the parameter D such that

$$U = \tau_w \Pi, \quad b_w = \frac{\sqrt{2D}}{\tau_w}. \tag{49}$$

Here U and D are in units of $\mathrm{m^2s^{-1}}$. In terms of U and D, the strong-friction system from(16) can then be written as

$$dz = -U'(z)dt + \sqrt{2D}dW. \tag{50}$$

Given the dynamics in (50), the starting point for the asymptotics is the exact formula for the mean convective initiation time (e.g., Gardiner 2004)

$$T(z_o \to \mathrm{LFC}^+) = \frac{1}{D}\int_{z_o}^{\mathrm{LFC}^+}\left[e^{U(z)/D}\int_{-\infty}^{z} e^{-U(z')/D}dz'\right]dz, \tag{51}$$

where $\mathrm{LFC}^+ > \mathrm{LFC}$ is the absorbing barrier located just above the level of free convection (see bottom panel of Fig. 2). Let us define the scales of the system $[z]$, $[t]$, and $[w]$ as in Appendix A, and U is non-dimensionalized with the scale $[U] = \tau_w[\Pi]$. Here we note that the following relations hold:

$$\mu = \frac{D}{[U]}, \quad \frac{D}{([z]^2/[t]} = \frac{\tau_w}{[t]} = \lambda. \tag{52}$$

The asymptotic approximation is obtained with the use of the Laplace method. Denoting again with tildes the non-dimensional quantities, equation (51) can be re-written as

$$\begin{aligned}
&\tilde{T}(\tilde{z}_o \to \tilde{\mathrm{LFC}^+}) \\
&= \frac{1}{\lambda}\int_{\tilde{z}_o}^{\widetilde{\mathrm{LFC}^+}} e^{\mu^{-1}\tilde{U}(\tilde{z})}d\tilde{z}\int_{-\infty}^{\widetilde{\mathrm{LFC}^+}} e^{-\mu^{-1}\tilde{U}(\tilde{z}')}d\tilde{z}' \\
&\quad -\frac{1}{\lambda}\int_{\tilde{z}_o}^{\widetilde{\mathrm{LFC}^+}}\left[e^{\mu^{-1}\tilde{U}(\tilde{z})}\int_{\tilde{z}}^{\widetilde{\mathrm{LFC}^+}} e^{-\mu^{-1}\tilde{U}(\tilde{z}')}d\tilde{z}'\right]d\tilde{z}.
\end{aligned} \tag{53}$$

We note that the second term is integrated over the domain $\tilde{z}_o \le \tilde{z} \le \widetilde{\mathrm{LFC}^+}, \tilde{z} \le \tilde{z}' \le \widetilde{\mathrm{LFC}^+}$. It is important to choose LFC^+ close enough to LFC so that $U(\mathrm{LFC}^+) > U(z_o)$ (see Fig. 2). The potential $\tilde{U}$ is increasing from $\tilde{z}_o$ to $\widetilde{\mathrm{LFC}}$, which implies $\tilde{U}(\tilde{z}) - \tilde{U}(\tilde{z}') \le \tilde{U}(\widetilde{\mathrm{LFC}^+}) - \tilde{U}(\tilde{z}_o) < U(\widetilde{\mathrm{LFC}}) - \tilde{U}(\tilde{z}_o)$, leading us to the following inequality

$$\begin{aligned}
&\frac{1}{\lambda}\int_{\tilde{z}_o}^{\widetilde{\mathrm{LFC}^+}}\int_{\tilde{z}}^{\widetilde{\mathrm{LFC}^+}} e^{\mu^{-1}(\tilde{U}(\tilde{z})-\tilde{U}(\tilde{z}'))}d\tilde{z}'d\tilde{z} \\
&\le \frac{(\widetilde{\mathrm{LFC}^+} - \tilde{z}_o)^2}{2\lambda}e^{\mu^{-1}(\tilde{U}(\widetilde{\mathrm{LFC}^+})-\tilde{U}(\tilde{z}_o))}.
\end{aligned} \tag{54}$$

We will later see that the leading order term is exponentially increasing when $\mu \to 0$ with exponent $e^{\mu^{-1}(\tilde{U}(\widetilde{\mathrm{LFC}})-\tilde{U}(\tilde{z}_o))}$, and so the error above can be ignored.

The other terms are estimated as follows. The integral with the negative sign in the exponent reaches its maximum at $\tilde{z}' = \tilde{z}_o$ while the other expression with the negative exponent reaches its maximum at $\tilde{z} = \widetilde{\mathrm{LFC}}$. Using Laplace's method, we get the following asymptotic expansion as $\mu \to 0$

$$\begin{aligned}
&\int_{-\infty}^{\widetilde{\mathrm{LFC}^+}} e^{-\mu^{-1}\tilde{U}(\tilde{z}')}d\tilde{z}' = \sqrt{\frac{2}{\tilde{U}''(\tilde{z}_o)}}\mu^{1/2}\Bigg[1+ \\
&\quad + \left(\frac{5}{24}\frac{(\tilde{U}''(\tilde{z}_o))}{(\tilde{U}''(\tilde{z}_o))^2} - \frac{1}{8}\frac{\tilde{U}^{(4)}(\tilde{z}_o)}{(\tilde{U}''(\tilde{z}_o))^2}\right)\mu + O(\mu^2),\Bigg]
\end{aligned} \tag{55}$$

and

$$\begin{aligned}
&\int_{\tilde{z}_o}^{\widetilde{\mathrm{LFC}^+}} e^{\mu^{-1}\tilde{U}(\tilde{z})}d\tilde{z} = \sqrt{\frac{-2}{\tilde{U}''(\widetilde{LFC})}}\mu^{1/2}\Bigg[1+ \\
&+\left(\frac{-5}{24}\frac{(\tilde{U}''(\widetilde{LFC}))}{(\tilde{U}''(\widetilde{LFC}))^2} + \frac{1}{8}\frac{\tilde{U}^{(4)}(\widetilde{LFC})}{(\tilde{U}''(\widetilde{LFC}))^2}\right)\mu + O(\mu^2)\Bigg].
\end{aligned} \tag{56}$$

The mean convective initiation time is then asymptotically expanded as

$$\begin{aligned}
\tilde{T} = \frac{\mu}{\lambda}&e^{\mu^{-1}(\tilde{U}(\widetilde{\mathrm{LFC}})-\tilde{U}(\tilde{z}_o))}\sqrt{\frac{2\pi}{\tilde{U}''(\tilde{z}_o)}}\sqrt{\frac{-2\pi}{\tilde{U}''(\widetilde{\mathrm{LFC}})}}\Bigg[1 \\
&+\left(\frac{-5}{24}\frac{(\tilde{U}''(\widetilde{LFC}))}{(\tilde{U}''(\widetilde{LFC}))^2} + \frac{1}{8}\frac{\tilde{U}^{(4)}(\widetilde{LFC})}{(\tilde{U}''(\widetilde{LFC}))^2} + \frac{5}{24}\frac{(\tilde{U}''(\tilde{z}_o))}{(\tilde{U}''(\tilde{z}_o))^2}\right. \\
&\left. - \frac{1}{8}\frac{\tilde{U}^{(4)}(\tilde{z}_o)}{(\tilde{U}''(\tilde{z}_o))^2}\right)\mu + O(\mu^2)\Bigg]
\end{aligned} \tag{57}$$

The dimensional form of this equation is presented in the main text in Section 6.

References

Bouchet F, Reygner J. 2016. Generalisation of the Eyring–Kramers transition rate formula to irreversible diffusion processes. *Annales Henri Poincaré* **17**(12): 3499–3532.

Brast M, Neggers RAJ, Heus T. 2016. What determines the fate of rising parcels in a heterogeneous environment? *J. Adv. Model. Earth Syst.* **8**(4): 1674–1690, doi:10.1002/2016MS000750.

D'Andrea F, Gentine P, Betts AK, Lintner BR. 2014. Triggering deep convection with a probabilistic plume model. *Journal of the Atmospheric Sciences* **71**(11): 3881–3901.

Deng Q, Smith LM, Majda AJ. 2012. Tropical cyclogenesis and vertical shear in a moist Boussinesq model. *J. Fluid Mech.* **706**: 384–412.

Emanuel KA. 1994. *Atmospheric convection*. Oxford University Press, New York.

Fraedrich K. 1985. On the distribution of cloud top heights based on stochastic forcing. *Tellus A* **37**(2): 176–184.

Gardiner CW. 2004. *Handbook of stochastic methods: for physics, chemistry & the natural sciences*, *Springer Series in Synergetics*, vol. 13. Springer–Verlag, Berlin.

Gentine P, Betts AK, Lintner BR, Findell KL, van Heerwaarden CC, D'Andrea F. 2013a. A probabilistic bulk model of coupled mixed layer and convection. part ii: Shallow convection case. *Journal of the Atmospheric Sciences* **70**(6): 1557–1576.

Gentine P, Betts AK, Lintner BR, Findell KL, van Heerwaarden CC, Tzella A, D'Andrea F. 2013b. A probabilistic bulk model of coupled mixed layer and convection. part i: Clear-sky case. *Journal of the Atmospheric Sciences* **70**(6): 1543–1556.

Grabowski WW, Jarecka D. 2015. Modeling condensation in shallow nonprecipitating convection. *J. Atmos. Sci.* **72**(12): 4661–4679.

Hernandez-Deckers D, Sherwood SC. 2016. A numerical investigation of cumulus thermals. *J. Atmos. Sci.* **73**(10): 4117–4136, doi:10.1175/JAS-D-15-0385.1.

Hernandez-Duenas G, Majda AJ, Smith LM, Stechmann SN. 2013. Minimal models for precipitating turbulent convection. *J. Fluid Mech.* **717**: 576–611, doi:10.1017/jfm.2012.597.

Higham DJ. 2001. An algorithmic introduction to numerical simulation of stochastic differential equations. *SIAM review* **43**(3): 525–546.

Hottovy SA, Stechmann SN. 2015. Threshold models for rainfall and convection: Deterministic versus stochastic triggers. *SIAM J. Appl. Math.* **75**: 861–884, doi:10.1137/140980788.

Jakob C, Siebesma AP. 2003. A new subcloud model for mass-flux convection schemes: Influence on triggering, updraft properties, and model climate. *Mon. Wea. Rev.* **131**(11): 2765–2778, doi:10.1175/1520-0493(2003)131%3C2765:ANSMFM%3E2.0.CO;2.

Kain JS, Fritsch JM. 1992. The role of the convective "trigger function" in numerical forecasts of mesoscale convective systems. *Meteorol. Atmos. Phys.* **49**(1): 93–106.

Lin J, Neelin J. 2000. Influence of a stochastic moist convective parameterization on tropical climate variability. *Geophys. Res. Lett.* **27**(22): 3691–3694, doi:10.1029/2000GL011964.

Majda A, Khouider B. 2002. Stochastic and mesoscopic models for tropical convection. *Proc. Natl. Acad. Sci. USA* **99**(3): 1123–1128.

Majda AJ, Xing Y. 2010. New multi-scale models on mesoscales and squall lines. *Commun. Math. Sci.* **8**: 113–144.

Metzner P, Schütte C, Vanden-Eijnden E. 2006. Illustration of transition path theory on a collection of simple examples. *The Journal of chemical physics* **125**(8): 084 110.

Neggers R, Siebesma A, Jonker H. 2002. A multiparcel model for shallow cumulus convection. *Journal of the atmospheric sciences* **59**(10): 1655–1668.

Romps DM, Charn AB. 2015. Sticky thermals: Evidence for a dominant balance between buoyancy and drag in cloud updrafts. *J. Atmos. Sci.* **72**(8): 2890–2901, doi:10.1175/JAS-D-15-0042.1.

Sherwood SC, Hernández-Deckers D, Colin M, Robinson F. 2013. Slippery thermals and the cumulus entrainment paradox. *J. Atmos. Sci.* **70**(8): 2426–2442, doi:10.1175/JAS-D-12-0220.1.

Simpson J, Wiggert V. 1969. Models of precipitating cumulus towers. *Mon. Wea. Rev* **97**(7): 471–489.

Stechmann SN, Neelin JD. 2011. A stochastic model for the transition to strong convection. *J. Atmos. Sci.* **68**: 2955–2970.

Stechmann SN, Neelin JD. 2014. First-passage-time prototypes for precipitation statistics. *J. Atmos. Sci.* **71**: 3269–3291.

Takahashi H, Luo Z. 2012. Where is the level of neutral buoyancy for deep convection? *Geophys. Res. Lett.* **39**(15).

Takahashi H, Luo ZJ. 2014. Characterizing tropical overshooting deep convection from joint analysis of CloudSat and geostationary satellite observations. *J. Geophys. Res.: Atmos.* **119**(1): 112–121.

Takahashi H, Luo ZJ, Stephens GL. 2017. Level of neutral buoyancy, deep convective outflow, and convective core: New perspectives based on 5 years of CloudSat data. *J. Geophys. Res.: Atmos.* **122**(5): 2958–2969.

Tao M. 2018. Hyperbolic periodic orbits in nongradient systems and small-noise-induced metastable transitions. *Physica D: Nonlinear Phenomena* **363**: 1–17.

Xu KM, Emanuel KA. 1989. Is the tropical atmosphere conditionally unstable? *Mon. Wea. Rev.* **117**(7): 471–1479.